Analytical Calculation of Electrodynamic Levitation Forces in a Special-Purpose Linear Induction Motor

Jacek F. Gieras, *Fellow, IEEE*, Jacek Mews, and Pawel Splawski

***Abstract*—A special transverse flux linear induction motor (LIM) with salient poles and nonferromagnetic secondary in the shape of a boat has been discussed. The secondary is suspended, propelled, and stabilized by the electromagnetic field. Equations of 2-D distribution of the electromagnetic field and force equations have been derived. A small-scale prototype has been built and tested. The electrodynamic suspension force obtained from analytical calculations has been compared with measurements. The obtained results have been critically discussed.**

***Index Terms*—Electromagnetic field, forces, induction motors, linear motors, magnetic levitation, transverse flux (TF) motors.**

NOMENCLATURE

a_R, a_X	Coefficients for including nonlinearity and hysteresis losses of ferromagnetic materials.
B	Magnetic flux density in teslas.
b_p	Width of salient pole in meters.
b_ν	Coefficient of Fourier series for B.
d	Thickness in meters.
d_{elm}	Distance between cores in meters (Fig. 1).
E	Electric field intensity in volts per meter.
F	Force in newtons.
f	Frequency in hertz.
H	Magnetic field intensity in amperes per meter.
I_{elm}	Electromagnet current in amperes.
I_{ph}	Phase current in amperes.
k_ν	Attenuation coefficient of electromagnetic field in per meter.
L_2	Axial length of the secondary in meters.
m	Number of phases.
p	Number of pole pairs.
R	Reluctance for magnetic flux in per henry.
R_{elm}	Resistance of a single electromagnet coil in ohms.
V_{elm}	Voltage across electromagnet coil in volts.
V_L	Line voltage in volts.
v	Linear synchronous velocity in meters per second.
v_2	Linear velocity of the secondary in meters per second.
w_2	Width of the secondary bottom.
X_{elm}	$= 2\pi f L_{\mathrm{elm}}$. Reactance of a single electromagnet coil in ohms.
α_ν	$= (a_R + ja_X)k_\nu$. Complex propagation constant in per meter.
β_ν	$= \nu\pi/\tau$. Constant (real number) in per meter.
Φ	Magnetic flux in webers.
κ_ν	$= (\alpha_\nu^2 + \beta_\nu^2)^{1/2}$. Complex propagation constant in per meter.
σ	Electric conductivity in siemens per meter.
τ	Pole pitch in the x-direction (traveling field) in meters.
τ_y	Pole pitch in the y-direction in meters.
μ_0	$= 0.4\pi \times 10^{-6}$ H/m. Magnetic permeability of free space.
μ_r	Relative magnetic permeability.
ν	Number of space harmonics.
ω	Angular frequency in radians per second.

Manuscript received July 12, 2011; revised October 21, 2011; accepted October 27, 2011. Date of publication November 11, 2011; date of current version January 20, 2012. Paper 2011-EMC-392.R1, presented at the 2011 IEEE International Electric Machines and Drives Conference, Niagara Falls, ON, Canada, May 15–18, and approved for publication in the IEEE TRANSACTIONS ON INDUSTRY APPLICATIONS by the Electric Machines Committee of the IEEE Industry Applications Society.

J. F. Gieras is with the Department of Electrical Engineering, University of Technology and Life Sciences, Bydgoszcz, 85-796, Poland, and also with Hamilton Sundstrand Applied Research, Rockford, IL 61125 USA (e-mail: jgieras@ieee.org).

J. Mews is with the Department of Electrical Engineering, University of Technology and Life Sciences, Bydgoszcz, 85-796, Poland, and also with the Technology Department, Gzelle Ltd., Osie, 86-150, Poland (e-mail: jacek.mews@interia.pl).

P. Splawski is with Saturn Management Ltd., Swiecie, 86-100, Poland (e-mail: splawik12@gmail.com).

Color versions of one or more of the figures in this paper are available online at http://ieeexplore.ieee.org.

Digital Object Identifier 10.1109/TIA.2011.2175881

I. INTRODUCTION

THERE ARE many types of electrodynamic levitation (EDL) devices [2], [3], [5], [6], [9]–[14]. Transverse flux (TF) linear induction motors (LIMs) can produce EDL force in addition to the thrust. In comparison with longitudinal flux (LF) LIMs, TF LIMs are easy to wound (salient poles), easy to cool (each coil is wound on a separate core), easy to transport (long primary unit made of small E- or U-cores), and cost-effective machines due to less winding and ferromagnetic-core materials for the same forces in comparison with their LF counterparts.

There were several attempts to use LIMs for noncontacting conveyance of steel plates [1], [11], [14]. A combined propulsion and lift system using attractive forces produced by a TF LIM has been proposed in [11]. With the dc-biased ac feeding to the TF LIM, a steel plate has been stably and efficiently supported [11]. Separate electromagnets for levitation and TF LIM for conveyance have been investigated in [1]. The mechanism to generate the thrust was to use the inclination of steel plate in the magnetic field of an E-shaped ferromagnetic-core electromagnet [1]. An image-based online gap-detection scheme for levitated steel-plate conveyance system in steel mills has been studied in [14]. Stable operation and low-noise

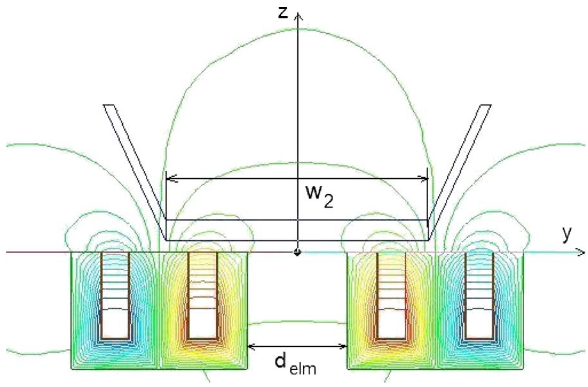

Fig. 1. Suspension of the conductive nonferromagnetic secondary in the shape of a boat with flat bottom in the magnetic field produced by a TF LIM (cross section).

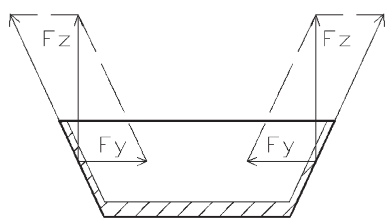

Fig. 2. Production of lateral stabilization forces F_y acting on the secondary.

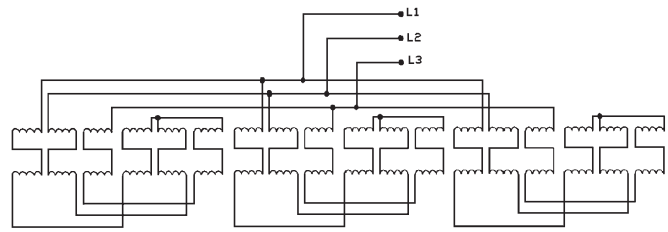

Fig. 3. Connection diagram of the primary coils to obtain unidirectional traveling magnetic field along the whole track (primary). Coils are wye connected with three parallel current paths per phase.

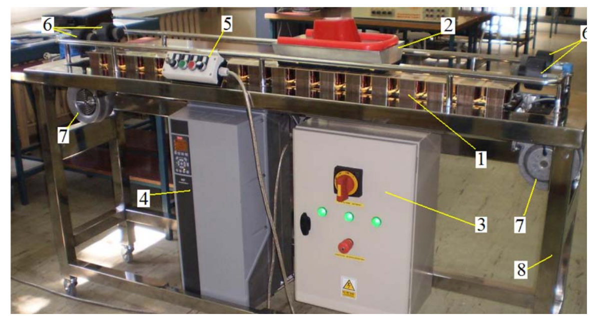

Fig. 4. Prototype of TF LIM with electrodynamically suspended secondary. (1) Primary (electromagnets). (2) Secondary. (3) Main switch and safety switch box. (4) Solid-state inverter. (5) Control unit. (6) Limit sensors. (7) Blowers. (8) Frame.

environment are the main objectives for the industrial steel-plate conveyance systems. In this paper, EDL forces [2], [3], [5]–[7], [9], [10], [12], [13] in a small-scale prototype of a TF LIM have been analyzed.

II. Prototype of TF LIM

If a flat primary winding, e.g., of a flat LIM, is fed with an ac current, a conductive paramagnetic or diamagnetic plate will be suspended above the primary core [2], [3], [5]–[7], [12], [13]. Without any lateral stabilization, e.g., with the aid of additional windings, the plate will be in the state of neutral equilibrium.

In the case of polyphase excitation, a traveling magnetic field produced by the primary winding will be moving the nonferromagnetic plate along the pole pitch overcoming only the air friction. The normal (suspension) force will be greater under action of the traveling magnetic field, because eddy currents are induced in the conductive plate by both transformer action and linear motion effects. Lateral stabilization forces will be produced if the conductive plate (the secondary) is appropriately shaped. It is possible to design the secondary as a "vehicle" suspended and propelled by the electromagnetic field of a LIM. Figs. 1 and 2 show the secondary shaped as a boat with flat bottom of a TF LIM [6], [7], [12].

The primary of the TF LIM consists of 36 electromagnets with E-shape cores distributed in two rows. The length of the track is 1450 mm, and its width is 216 mm. The dimensions of the E-shape cores are as follows: 56-mm height, 84-mm width, 40-mm thickness, 28-mm width of the center leg, 14-mm width of the external leg, and 14-mm height of the bottom yoke. The distance between two parallel rows of electromagnets $d_{\mathrm{elm}} = 48$ mm. The number of turns per electromagnet is $N = 177$, and the diameter of round wire without insulation is 1.3 mm. The class of insulation is 220 °C. The current density at 20 A *rms* is 15 A/mm^2. A forced air cooling system with an electric motor-driven blower has been applied. The maximum airflow is 255 m^3/h.

The connection diagram of electromagnet coils is shown in Fig. 3. There are four coils in series and three parallel current paths per phase (wye connection), so that the line voltage

$$V_L = 4\sqrt{3}V_{\mathrm{elm}} \quad (1)$$

and the phase/line current

$$I_{\mathrm{ph}} = I_L = 3I_{\mathrm{elm}} \quad (2)$$

where V_{elm} is the voltage at the terminals of a single electromagnet coil and I_{elm} is the electromagnet coil current.

The coils in Fig. 3 are wye connected in such a way as to obtain the traveling magnetic field along the whole length of the primary. It is also possible to connect the coils to produce only a pulsating magnetic field (single-phase excitation) or two traveling fields in opposite directions. Thus, in the second case, the secondary is kept in the stable center position of the track [7], [12].

The secondary in the shape of a boat with flat bottom made of aluminum alloy with an electric conductivity of 25.4×10^6 S/m at 20 °C has the following dimensions: length $L_2 = 340$ mm, width of the bottom $w_2 = 125$ mm, thickness of the bottom $d_2 = 10$ mm, 65-mm height, and sides inclined by 65°. All dimensions have been selected experimentally to obtain the best lateral stabilization [6]. The prototype of the TF LIM with electromagnetically suspended secondary is shown in Figs. 4 and 5. The primary is fed from a variable-voltage variable-frequency inverter.

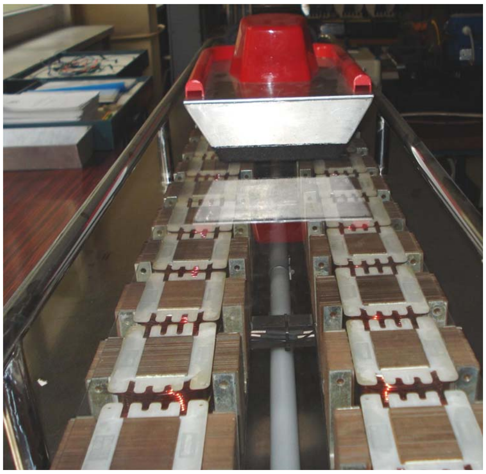

Fig. 5. Aluminum alloy secondary suspended electrodynamically above the salient-pole primary (an array of electromagnets).

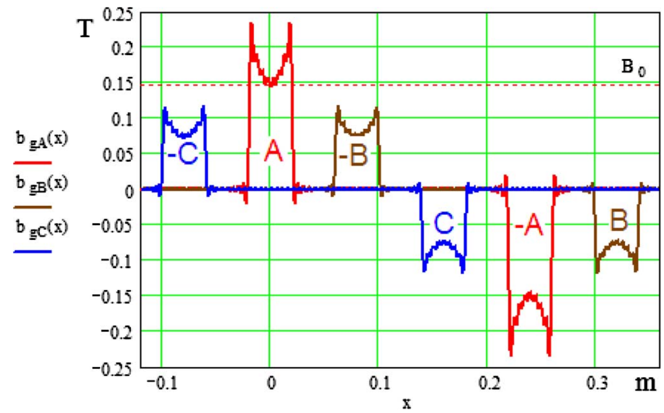

Fig. 6. Distribution of the magnetic flux density waveform at the active surface of the primary in the x-direction for three-phase excitation, $V_L = 300$ V, and $f = 50$ Hz. $B_0 = 0.15$ T according to measurements.

III. Consequences of Open Magnetic Circuit

The E-shaped cores of electromagnets have an open magnetic circuit. Magnetic flux penetrates through the air above the active surface of electromagnets. Since the secondary is non-ferromagnetic and the equivalent air gap is large, even with the presence of the secondary, the magnetic circuit of the primary remains open. The consequences are as follows.

1) The reactive (magnetizing) component of the current is predominant, and the core loss current can be neglected (Appendix I).
2) The power consumption by the track (primary) is high (Appendix II).
3) The current, input power, and power factor practically do not depend on the presence or absence of the secondary (Appendix II).
4) The magnetic flux density in the air gap is low and does not exceed 0.25 T (0.15 T at $V_L = 300$ V).

IV. Magnetic Field Excited by the Primary

The normal component of the magnetic flux density waveform in the x-direction excited by the primary system can be expressed with the aid of Fourier series

$$b_g(x) = \sum_{\nu=1}^{\infty} B_0 b_\nu \cos\left(\nu \frac{\pi}{\tau} x\right) \tag{3}$$

where $\nu = 1, 3, 5, 7, \ldots$ represents the space harmonics. The first harmonic $\nu = 1$ is

$$b_{g1}(x) = B_0 b_{\nu=1} \cos\left(\frac{\pi}{\tau} x\right). \tag{4}$$

The following Fourier coefficient provides the best approximation of the magnetic flux density distribution [5], [7]:

$$b(\nu) = \frac{4}{\pi} \frac{1}{(2\alpha/b_p)^2 + \beta_\nu^2} \left[\frac{2\alpha}{b_p} \sinh(\alpha) \sin\left(\nu\pi \frac{\tau - b_p}{2\tau}\right) + \beta_\nu \cosh(\alpha) \cos\left(\nu\pi \frac{\tau - b_p}{2\tau}\right)\right] \sin\left(\nu \frac{\pi}{2}\right) \tag{5}$$

where $b_p = 40$ mm is the primary pole width (in the x-direction), τ is the pole pitch ($\tau = 240$ mm in the case of three-phase excitation), and

$$\beta_\nu = \nu \frac{\pi}{\tau} \tag{6}$$

is the real constant dependent on the periodic distribution of the electromagnetic field in the x-direction. The parameter $\alpha = 0$ if the magnetic flux density over the salient pole has a constant value along the x coordinate, and $\alpha = 1$ if the magnetic flux density over the salient pole changes according to cosh law.

For the three-phase sequence of currents $A, -B, C, -A, B, \ldots, V_L = 300$ V, and $f = 50$ Hz, the magnetic flux density waveform traveling in the x-direction at the surface of the primary system ($z = 0$) is shown in Fig. 6. According to (1), the corresponding voltage at the terminals of a single electromagnet coil is $V_{\text{elm}} = 43.3$ V. The corresponding magnetic flux density on the surface of the center leg in its central line of the electromagnet (Appendix I) is $B_0 = 0.15$ T. The analytical method of calculation of B_0 is given in Appendix I. The calculated flux density has been verified with experimental tests (Fig. 17; Appendix I).

Similarly, the distribution of the magnetic flux density normal component in the y-direction can be found, i.e.,

$$b_g(y) = \sum_{n=1}^{\infty} B_0 b_n \cos\left(n \frac{\pi}{\tau_y} y\right) \tag{7}$$

where the Fourier coefficient [5]

$$b_n = \frac{4}{\tau_y} \left\{ \left[\frac{c_p}{c_p^2 + \eta_n^2} \sinh(\alpha) - \frac{6}{\eta_n^4} \frac{1}{b_t^3} \cosh(\alpha) + \frac{3}{\eta_n^3} \frac{1}{b_t} \cos ch(\alpha)\right] \sin(\eta_n b_t) + \left[\frac{\eta_n}{c_p^2 + \eta_n^2} + \frac{6}{\eta_n^3} \frac{1}{b_t^2} - \frac{1}{\eta_n}\right] \cosh(\alpha) \cos(\eta_n b_t) \right\}, \tag{8}$$

$$\eta_n = n \frac{\pi}{\tau_y}; \qquad c_p = \frac{2\alpha}{b_p}; \qquad b_t = \frac{\tau_y - b_p}{2} \tag{9}$$

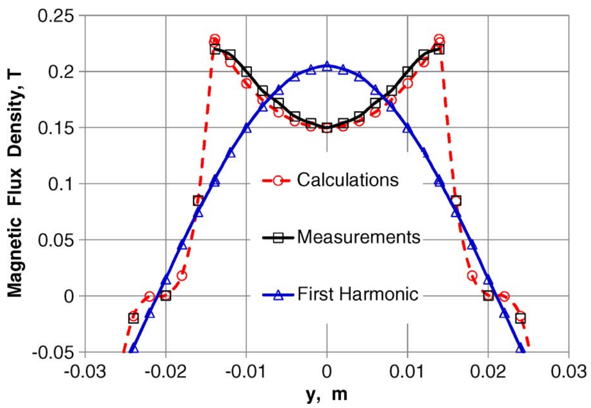

Fig. 7. Distribution of the normal component of magnetic flux density and its first harmonic at the active surface of the primary in the y-direction for $V_L =$ 300 V and $f = 50$ Hz. See also Fig. 17.

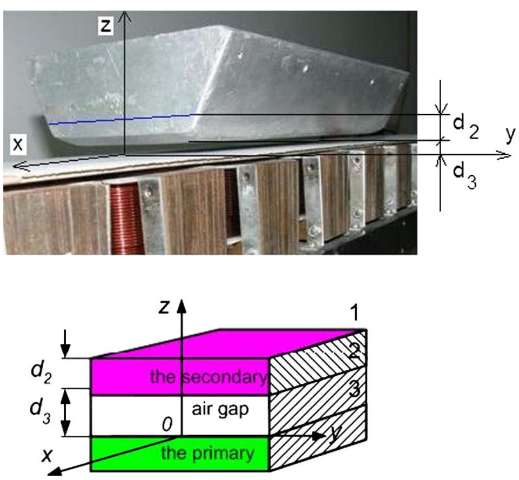

Fig. 8. Three-layer model for 2-D analysis of the electromagnetic field. (1) Top layer is air half-space. The thrust is in the x-direction, the suspension force is in the z-direction, and the lateral stabilization forces are in the y-direction.

where $n = 1, 3, 5, 7, \ldots$ represents the space harmonics of the magnetic flux density distribution in the y-direction and $\tau_y =$ 42 mm is the half period of the magnetic flux density wave.

The magnetic flux density distribution in the y-direction at the surface of the primary core $(z = 0)$ obtained from calculations according to (7)–(9) and measurements at the input voltage $V_L = 300$ V and frequency $f = 50$ Hz (one electromagnet) is plotted in Fig. 7.

In the 2-D analysis of the electromagnetic field, the magnetic flux density in the y-direction is assumed to be constant.

V. Electromagnetic Field and Forces

1) Equations of Electromagnetic Field Distribution: The three-layer model for the derivation of the 2-D electromagnetic field equations is shown in Fig. 8. The first layer 1 is the air half-space, the second layer 2 is the secondary, and the third layer 3 is the air gap (mechanical clearance) between the primary and the secondary. The magnetic field in the air is described by Laplace's equations, while in the conductive secondary, it is described by the Helmholtz equation. Assuming that the primary is with salient poles and using boundary conditions for tangential and normal components at $z = 0$, $z = d_3$, and $z = d_2 + d_3$, equations of the 2-D electromagnetic field distribution in the secondary (region $d_3 \le z \le d_2 + d_3$) are [5], [8], [9]

$$H_{x\nu 2}^{(3)} = (\pm j)\frac{1}{\beta_\nu}\kappa_{\nu 2}\frac{1}{\mu_3}\frac{1}{M_{\nu 3}^{(3)}}B_\nu b_\nu e^{\mp j\beta_\nu x} \times \left[\frac{\kappa_{\nu 1}}{\kappa_{\nu 2}}\cosh\left[\kappa_{\nu 2}(z - d_2 - d_3)\right] - \frac{\mu_1}{\mu_2}\sinh\left[\kappa_{\nu 2}(z - d_2 - d_3)\right]\right] \quad (10)$$

$$H_{z\nu 2}^{(3)} = \frac{1}{\mu_3}\frac{1}{M_{\nu 3}^{(3)}}B_\nu b_\nu e^{\mp j\beta_\nu x} \times \left[\frac{\mu_1}{\mu_2}\cosh\left[\kappa_{\nu 2}(z - d_2 - d_3)\right] - \frac{\kappa_{\nu 1}}{\kappa_{\nu 2}}\sinh\left[\kappa_{\nu 2}(z - d_2 - d_3)\right]\right] \quad (11)$$

$$E_{y\nu 2}^{(3)} = j\omega_{\nu 2}\mu_2(\mp j)\frac{1}{\beta_\nu}\frac{1}{M_{\nu 3}^{(3)}}B_\nu b_\nu e^{\mp j\beta_\nu x} \times \left[\frac{\mu_1}{\mu_2}\cosh\left[\kappa_{\nu 2}(z - d_2 - d_3)\right] - \frac{\kappa_{\nu 1}}{\kappa_{\nu 2}}\sinh\left[\kappa_{\nu 2}(z - d_2 - d_3)\right]\right] \quad (12)$$

where

$$M_{\nu 3}^{(3)} = \frac{\kappa_{\nu 2}}{\kappa_{\nu 3}}M_{\nu 2}^{(2)}\sinh(\kappa_{\nu 3}d_3) + \frac{\mu_2}{\mu_3}W_{\nu 2}^{(2)}\cosh(\kappa_{\nu 3}d_3) \quad (13)$$

$$M_{\nu 2}^{(2)} = \frac{\kappa_{\nu 1}}{\kappa_{\nu 2}}\cosh(\kappa_{\nu 2}d_2) + \frac{\mu_1}{\mu_2}\cosh(\kappa_{\nu 2}d_2) \quad (14)$$

$$W_{\nu 2}^{(2)} = \frac{\mu_1}{\mu_2}\cosh(\kappa_{\nu 2}d_2) + \frac{\kappa_{\nu 1}}{\kappa_{\nu 2}}\sinh(\kappa_{\nu 2}d_2). \quad (15)$$

The sign "+" corresponds to the forward-traveling field ($\nu = 1, 7, 13, 19, \ldots$), the sign "−" corresponds to the backward-traveling magnetic field ($\nu = 5, 11, 17, 23, \ldots$), B_ν is the peak value of the magnetic flux density at the surface of the primary $(z = 0)$, β_ν is the real constant dependent on the periodic distribution of the electromagnetic field in the x-direction (6), and κ_ν is the propagation constant (complex in the case of a conductive medium), i.e.,

$$\kappa_{\nu 1} = \kappa_{\nu 3} = \beta_\nu \quad (16)$$

$$\kappa_{\nu 2} = \sqrt{\alpha_{\nu 2}^2 + \beta_\nu^2} = (a_{R\nu} + ja_{X\nu})k_{\nu 2} \quad (17)$$

$$\alpha_{\nu 2} = \sqrt{j\omega_{\nu 2}\mu_0\mu_{r2}\sigma_2} = (a_R + ja_X)k_{\nu 2} \quad (18)$$

$$a_{R\nu} = \frac{1}{\sqrt{2}}\sqrt{\sqrt{4 + \frac{\beta_\nu^4}{k_{\nu 2}^4}} + \frac{\beta_\nu^2}{k_{\nu 2}^2}} \quad (19)$$

$$a_{X\nu} = \frac{1}{\sqrt{2}}\sqrt{\sqrt{4 + \frac{\beta_\nu^4}{k_{\nu 2}^4}} - \frac{\beta_\nu^2}{k_{\nu 2}^2}}. \quad (20)$$

In (10)–(12), the νth harmonic normal component of the magnetic flux density at the active surface of the primary unit is described by the following equations:

- for a single-phase $(m = 1)$ TF LIM

$$b_g(x) = 0.5B_0 b_\nu \left[e^{j(\omega_\nu^+ t - \beta_\nu x)} + e^{j(\omega_\nu^- t + \beta_\nu x)}\right] \tag{21}$$

- for a three-phase $(m = 3)$ TF LIM

$$b_g(x) = 0.5B_0 b_\nu \left[e^{j(\omega_\nu^+ t - \beta_\nu x)}(1 + a^{\nu+2} + a^{2\nu+1}) + e^{j(\omega_\nu^- t + \beta_\nu x)}(1 + a^{2\nu+2} + a^{\nu+1})\right]. \tag{22}$$

The subscript "+" denotes the forward-traveling field $(\nu = 1, 7, 13, 19, \ldots)$, and the superscript "−" denotes the backward-traveling magnetic field $(\nu = 5, 11, 17, 23, \ldots)$. Also

- for forward-traveling magnetic field

$$B_\nu^+ = \begin{cases} 0.5B_0, & \text{if } m = 1 \\ 0.5B_0(1 + a^{\nu+2} + a^{2\nu+1}), & \text{if } m = 3 \end{cases} \tag{23}$$

- for backward-traveling magnetic field

$$B_\nu^- = \begin{cases} 0.5B_0, & \text{if } m = 1 \\ 0.5B_0(1 + a^{2\nu+2} + a^{\nu+1}), & \text{if } m = 3 \end{cases} \tag{24}$$

where m is the number of phases and $a = \exp(j2\pi/3)$.

In (19) and (20), $a_R = a_X = 1$ and $\mu_{r2} = 1$ because the secondary must be nonferromagnetic [5]. For a ferromagnetic secondary, $a_R \approx 1.45$ and $a_X \approx 0.85$ [4], [8], [9]. Complex propagation constant, magnetic permeability, and coefficients a_R and a_X are explained in Appendix III.

The pulsation for the νth space harmonic of eddy currents in the secondary is

$$\omega_{\nu 2} = \omega \pm \beta_\nu v_2 = 2\pi f \pm \beta_\nu v_2 \tag{25}$$

where v_2 is the linear velocity of the secondary, and the attenuation factor of the electromagnetic field in the secondary is

$$k_\nu = \sqrt{\frac{\omega_{\nu 2}\mu_0\mu_{r2}\sigma_2}{2}}. \tag{26}$$

Equation (13) covers all possible methods of feeding of LIMs. For a dc current, $\omega = 2\pi f = 0$, $v_2 \neq 0$, and $\omega_{\nu 2} = \pm\beta_\nu v_2$. For an ac current, $\omega \neq 0$ and $v_2 = 0$ for the pulsating field, $v_2 \neq 0$ and $\omega_{\nu 2} = \omega - \beta_\nu v_2$ for the forward-traveling field, and $v_2 \neq 0$ and $\omega_{\nu 2} = \omega + \beta_\nu v_2$ for the backward-traveling field (Appendix IV).

2) Electrodynamic Forces: Electrodynamic forces on the secondary per unit area in the x- and z-directions can be found using the Maxwell stress tensor, i.e.,

$$f_{x\nu} = -0.5\mu_0 \Re e\left[H_{z\nu} H_{x\nu}^*\right]_{z=d_3} \tag{27}$$

$$f_{z\nu} = 0.5\mu_0 \Re e\left[0.5 H_{z\nu} H_{z\nu}^* - 0.5 H_{x\nu} H_{x\nu}^*\right]_{z=d_3}. \tag{28}$$

Hence, the total forces on the secondary

$$F_x = S_{\text{sec}} \sum_{\nu=1}^{\infty} f_{x\nu} \tag{29}$$

$$F_z = S_{\text{sec}} \sum_{\nu=1}^{\infty} f_{z\nu}. \tag{30}$$

Since only a part of the secondary bottom is under action of the electromagnetic field, the active surface of the secondary bottom is $S_{\text{sec}} = 2p\tau(w_2 - d_{\text{elm}})$ (Fig. 1). The number $2p$ of pole pitches τ must correspond to the length of the secondary L_2 in the x-direction. Thus, the equivalent surface of the secondary bottom in (29) and (39) is $S_{\text{sec}} = L_2(w_2 - d_{\text{elm}}) = 0.34(0.125 - 0.048) = 0.026$ m^2, where $L_2 = 0.34$ m, $w_2 = 0.125$ m, and $d_{\text{elm}} = 0.048$ m.

VI. Calculations Versus Tests

The magnetic flux density excited by the primary is a function of the input voltage. The magnetic flux density B_0 at the surface of the primary core as a function of the input *rms* line voltage V_L has been found in Appendix I. Analytical approach has been verified with the test data (Fig. 17).

For calculation of the thrust F_x and suspension force F_z given by (29) and (30), the conductivity of the secondary has to be corrected by including the temperature effect and edge effect. The edge effect coefficient [8], [9]

$$k_{z\nu} \approx 1 + 0.5\frac{1}{\nu}\frac{\tau}{L_e} \tag{31}$$

can be found from the distribution of eddy currents in the secondary. Since the pole pitch for higher space harmonics is τ/ν, the edge effect coefficient is a function of the number ν of higher space harmonics. The length of eddy current paths in the y-direction is $L_e = 0.5(w_2 - d_{\text{elm}}) = 0.5(0.125 - 0.048) = 0.039$ m. It corresponds to the axial length of a rotor, e.g., in a solid rotor induction machine. Including both the temperature and edge effects, the equivalent conductivity of the secondary (second layer in Fig. 8) is

$$\sigma_2(\nu) \approx \frac{\sigma_{\text{Al}20}}{1 + 0.0039(\theta_2 - 20)} \frac{1}{\left(1 + 0.5\frac{1}{\nu}\frac{\tau}{w_2}\right)^2}. \tag{32}$$

The conductivity of aluminum alloy secondary at 20 °C is $\sigma_{\text{Al}20} = 25.4 \times 10^6$ S/m, θ_2 is the temperature of the secondary, $\tau = 0.24$ m is the pole pitch in the x-direction for three-phase excitation, and $w_2 = 0.125$ m (Fig. 1) is the secondary width in the y-direction. For $\sigma_{\text{Al}20} = 25.4 \times 10^6$ S/m, $\nu = 1$, and $\theta_2 = 75$ °C, the equivalent conductivity (32) of the secondary is $\sigma_2(\nu = 1) = 1.234 \times 10^6$ S/m.

Calculations and test results of tangential force F_x and axial force F_z are compared in Figs. 9–11. The tangential force F_x has been measured for stationary secondary (velocity $v_2 = 0$ m/s) using a string, pulley, and weighs. For measurement of the normal suspension force, the weight of the secondary was adjusted to 23.15 N. Then, the voltage was gradually increased from 240 to 420 V. The air gap d_3 was measured with the aid of an optical sensor. A temperature sensor was installed in the bottom of the secondary to keep its temperature $\theta_2 = 75° = const.$ Measurements are difficult, because tests must be frequently interrupted not to allow the temperature of the secondary to exceed $\theta_2 = 75$ °C. Two traveling fields in opposite directions have been excited.

The influence of the temperature on the suspension force F_z is shown in Fig. 12. In practical control systems with TF

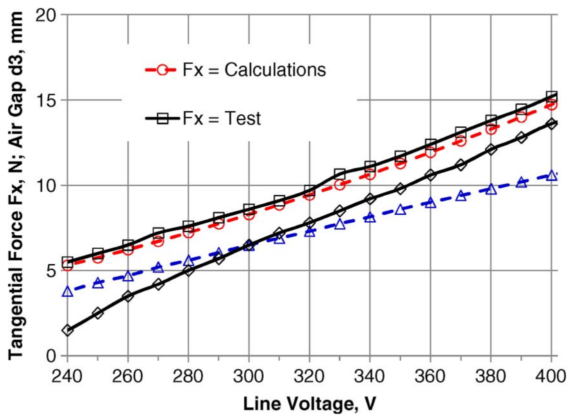

Fig. 9. Comparison of calculations of the thrust (tangential force) F_x and air gap d_3 with measurements at $f = 50$ Hz, velocity $v_2 = 0$, and $\theta_2 = 75\ ^\circ$C.

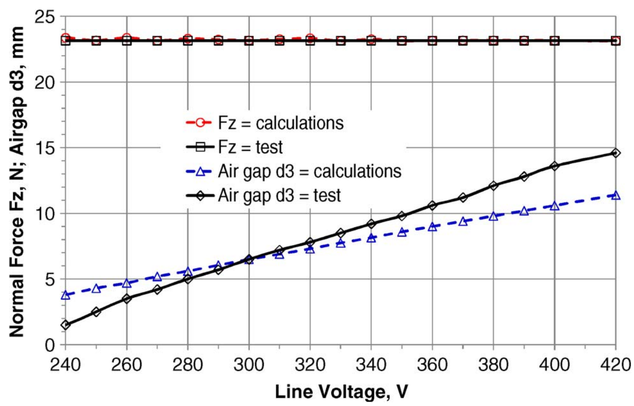

Fig. 10. Comparison of calculations of the suspension force F_z and air gap d_3 with measurements at $f = 50$ Hz, velocity $v_2 = 0$ m/s, and $\theta_2 = 75\ ^\circ$C.

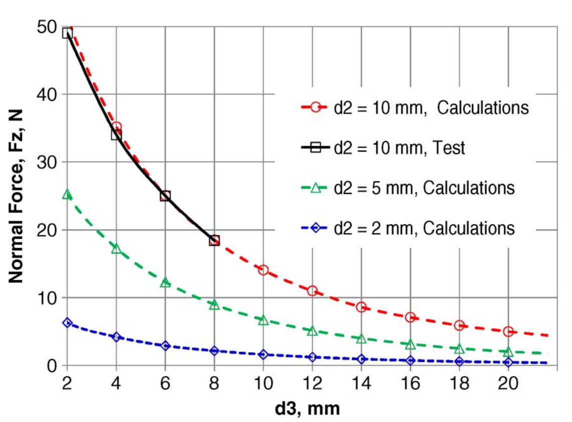

Fig. 11. Electrodynamic suspension force as a function of the air gap d_3 for three different thicknesses $d_2 = 10,\ 5,$ and 2 mm of the secondary bottom at 300 V and 50 Hz. Calculation results on the basis of (30).

LIM shown in Figs. 4 and 5, a contactless temperature sensor is required, e.g., an infrared temperature sensor.

The electric conductivity of the material of the secondary has a significant influence on the suspension force F_z. On the other hand, the secondary made of copper ($\sigma_{\rm Cu20} \approx 57 \times 10^6$ S/m at 20 °C) is about 3.26 times heavier than the aluminum secondary of the same size.

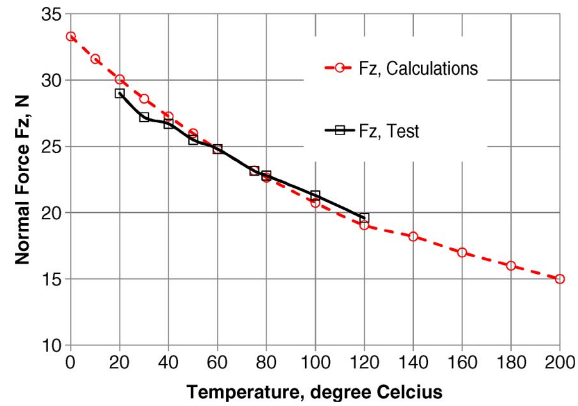

Fig. 12. Influence of the temperature of the secondary on the suspension force F_z. Calculation results for $V = 300$ V *rms*, $f = 50$ Hz, $d_2 = 10$ mm, and $d_3 = 6.5$ mm.

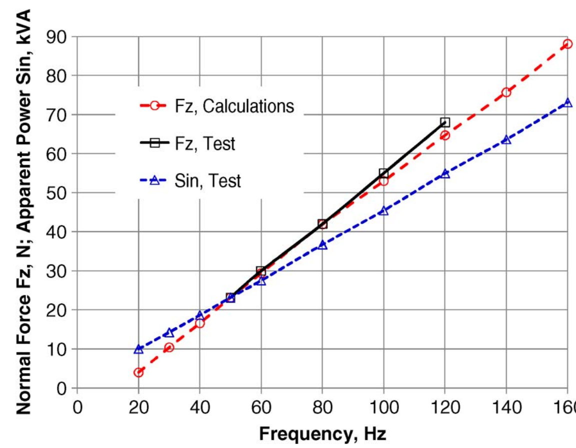

Fig. 13. Influence of the input frequency on the suspension force. F_z and input apparent power $S_{\rm in}$. Calculation results for $V = 300$ V *rms*, $\theta_2 = 75\ ^\circ$C, $d_2 = 10$ mm, and $d_3 = 6.5$ mm.

In calculation of tangential force F_x and axial force F_z, both the fundamental harmonic $\nu = 1$ and higher harmonics $\nu = 5, 7, 11, 13, \ldots, 103$ have been taken into account.

The force density, i.e., the force per mass, for this type of TF LIM is low. The thrust density, i.e., tangential force per mass, of the secondary (neglecting the mass of the primary) is $f_{x\rm sec} = 4.3$ N/kg, and the normal suspension force density is $f_{z\rm sec} = 9.8$ N/kg. Including the portion of the primary underneath the secondary (ten electromagnets in two parallel rows), the thrust density is $f_x = 0.6$ N/kg, and the normal suspension force density is $f_z = 1.8$ N/kg. The aforementioned force densities correspond to $d_2 = 10$ mm, $d_3 = 6.5$ mm, $f = 50$ Hz, $V_L = 300$ V, and $B_0 = 0.15$ T. In electromagnetic levitation systems (attractive forces), force densities can reach hundred newtons per kilogram.

The normal force as a function of the input frequency is shown in Fig. 13. Calculations and measurements have been done for $B_0 = 0.15\ {\rm T} = const$, constant phase current $I_{\rm ph} = 44.65$ A, and constant input real power $P_{\rm in} = 4330$ W. As the frequency increases, the apparent power $S_{\rm in}$ increases, and the power factor decreases. The theoretical power factor $\cos\varphi = 0.302$ at $f = 20$ Hz, $\cos\varphi = 0.187$ at 50 Hz, and $\cos\varphi = 0.059$

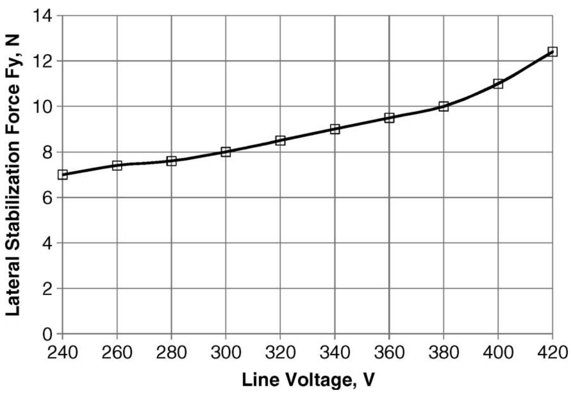

Fig. 14. Lateral stabilization force F_y versus line voltage V_L at $F_z = 23.15$ N. Test results for $f = 50$ Hz, $\theta_2 = 75$ °C, $d_2 = 10$ mm, and $d_3 = 6.5$ mm.

at 160 Hz. When the input frequency is doubled, the force F_z increases more than twice (Fig. 13).

The error in analytical calculation of lateral stabilization force F_y for the secondary in the shape of a boat using both the Maxwell stress tensor and Lorentz equation was over 100%. This was due to the complex shape of the secondary (Fig. 2). Equations (10)–(12) have been derived for the secondary in the shape of a rectangular plate. Therefore, only test results of the lateral stabilization force F_y have been shown (Fig. 14).

The agreement between analytical calculations and measurements of the thrust F_x and suspension force F_z is sufficient (Figs. 9–11) for the design and calculation of performance characteristics of special TF LIMs with electrodynamically suspended secondary. The discrepancy (Figs. 9 and 10) between calculation and measurements of the air gap d_3 corresponding to given values of F_x and F_z is, first of all, due to a certain error between the distribution of the electromagnetic field described by analytical equations (10)–(12) and the true distribution of the electromagnetic field. Two-dimensional model and physical simplifications in the analysis can also contribute to errors in analytical calculations.

VII. Conclusion

Analytical equations for the thrust and normal suspension forces in a special TF LIM with the secondary propelled, levitated, and stabilized electromagnetically have been derived and verified experimentally on a small-scale prototype. Comparison between calculations and measurements shown in Figs. 9–13 confirms an acceptable accuracy of the analytical approach. The 2-D finite-element method (FEM) (*MagNet Infolytica*) analysis gives $\pm 10\%$ error between computation and test results. The FEM analysis results have not been published in this paper.

The higher the magnetic flux density for $d_2 = const$ and $d_3 = const$, the higher the thrust, suspension force, and lateral stabilization forces.

The suspension force is very sensitive to the temperature of the secondary (Fig. 12). The suspension force increases with the input frequency at constant voltage excitation (Fig. 13).

It has been found that the main reason for the secondary vibration is higher time harmonics produced by the inverter. An inverter with low content of higher time harmonics is necessary for vibration-free, noiseless, and stable operation of this type of the TF LIM.

So far, the prototype of the TF LIM (Figs. 4 and 5) is used only for education and public awareness of the EDL effect (teaching at graduate level, university *open door*, science festivals, exhibitions, science education, amusement parks, etc.).

Precision manufacturing industry and defense forces have shown interest in TF LIMs with the secondary suspended electrodynamically. One of the possible applications is noncontacting conveyance of paramagnetic and diamagnetic conductive bodies, particularly plates and slabs where the force density and energy consumption is not important.

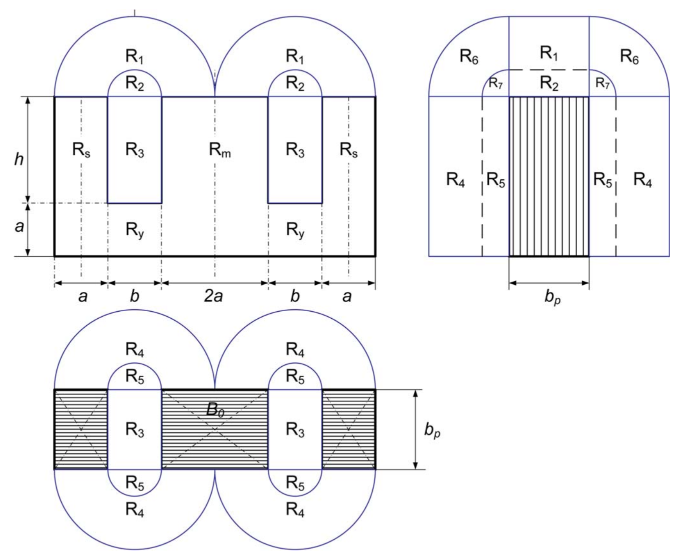

Fig. 15. Division of the magnetic circuit of the E-type electromagnet into simple solids.

Appendix I
Magnetic Flux Density Excited by Electromagnets

With sufficient accuracy, the normal component of the magnetic flux density at the surface of the center leg of the electromagnet can be found using the reluctance network approach [15]. Fig. 15 shows the E-type core of the electromagnet with the magnetic flux in the open space divided into simple solids.

The reluctance for the magnetic flux of each solid is expressed by the following equations [10, p. 445]:

1) reluctance of the center leg of the core

$$R_m = \frac{h + 0.5a}{\mu_0 \mu_{\mathrm{rc}} S_g} \tag{33}$$

2) reluctance of the side leg of the core

$$R_s = \frac{h + 0.5a}{0.5\mu_0 \mu_{\mathrm{rc}} S_g} \tag{34}$$

3) reluctance of the yoke

$$R_y = \frac{b + a}{0.5\mu_0 \mu_{\mathrm{rc}} S_g} \tag{35}$$

4) reluctance of a hollow half cylinder on the top of the core

$$R_1 = \frac{\pi}{\mu_0 \ln(1 + 2a/b) b_p} \tag{36}$$

5) reluctance of a solid half cylinder on the top of the core

$$R_2 = \frac{1}{0.26 \mu_0 b_p} \tag{37}$$

6) reluctance of a rectangular cube between center and side legs

$$R_3 = \frac{b}{\mu_0 h b_p} \tag{38}$$

7) reluctance of a hollow half cylinder between center and side legs

$$R_4 = \frac{\pi}{\mu_0 \ln(1 + 2a/b) h} \tag{39}$$

8) reluctance of a solid half cylinder between center and side legs

$$R_2 = \frac{1}{0.26 \mu_0 h} \tag{40}$$

9) reluctance of one quarter of solid shell at top corners

$$R_6 = \frac{4}{\mu_0 a} \tag{41}$$

10) reluctance of one quarter of sphere at top corners

$$R_7 = \frac{1}{0.077 \mu_0 b}. \tag{42}$$

In (33)–(35), μ_{rc} is the relative magnetic permeability of the ferromagnetic core, and $S_g = 2ab_p$ is the cross section of the center leg. For dimensions as in Fig. 15, the relative magnetic permeability μ_{rc} in each portion of the core is the same.

Reluctances (33)–(37) are reluctances for the main (useful) flux, while reluctances (38)–(42) are reluctances for leakage fluxes. Equivalent reluctances for the flux in the air are as follows:

- for the main flux

$$R_{12\mathrm{eq}} = \frac{1}{1/R_1 + 1/R_2} \tag{43}$$

- for leakage fluxes

$$R_{3\mathrm{eq}} = \frac{1}{1/R_3 + 2/R_4 + 2/R_5 + 2/R_6 + 2/R_7}. \tag{44}$$

Reluctances R_4–R_7 are at both sides of the core, so that there is $2/R_4, 2/R_5, \ldots$ in the denominator of (44).

For an open E-type core, the magnetizing current I_Φ is predominant, i.e., the core loss current (active component) $I_{\mathrm{Fe}} \ll I_\Phi$. Thus, the electromagnet current

$$I_{\mathrm{elm}} = \sqrt{I_{\mathrm{Fe}}^2 + I_\Phi^2} \approx I_\Phi \tag{45}$$

$$I_{\mathrm{elm}} = \frac{V_{\mathrm{elm}}}{\sqrt{R_{\mathrm{elm}}^2 + X_{\mathrm{elm}}^2}} \tag{46}$$

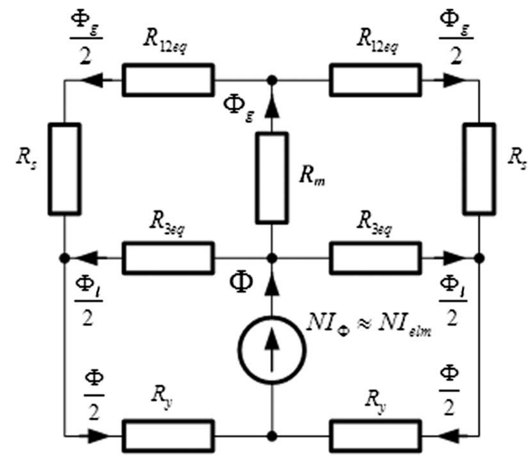

Fig. 16. Equivalent magnetic circuit of a single electromagnet: Φ is the total magnetic flux excited by the electromagnet coil, Φ_g is the main useful flux, Φ_l is the leakage flux, and NI_Φ is the magnetomotive force.

where R_{elm} is the resistance of the single electromagnet coil, X_{elm} is its reactance, and V_{elm} is the voltage at the electromagnet coil terminals. The main (useful) magnetic flux as a function of V_{elm} can be found as

$$\Phi_g = 2N \frac{V_{\mathrm{elm}}}{\sqrt{R_{\mathrm{elm}}^2 + X_{\mathrm{elm}}^2}} \frac{R_{3\mathrm{eq}}}{R_d} \tag{47}$$

where N is the number of turns, $R_{3\mathrm{eq}}$ is according to (44), and

$$R_d = 2R_m(R_{3\mathrm{eq}} + R_y) + (R_{12\mathrm{eq}} + R_s)(R_{3\mathrm{eq}} + R_y) + R_y R_{3\mathrm{eq}}. \tag{48}$$

Equations (47) and (48) have been derived using the equivalent reluctance network shown in Fig. 16. The normal component of the magnetic flux density at the surface of the center leg in its center line

$$B_0 = \frac{\Phi_g}{S_g}. \tag{49}$$

For $V_L = 300$ V and connection diagram as in Fig. 3, the voltage at the terminals of a single electromagnet $V_{\mathrm{elm}} = 300/(4\sqrt{3}) = 43.3$ V, the resistance at 75 °C $R_{\mathrm{elm}} = 0.543\ \Omega$, and inductance $L_{\mathrm{elm}} = 9.1$ mH. Both R_{elm} and L_{elm} have been obtained from measurements. It is also possible to estimate the $L_{\mathrm{elm}} = N^2/R_t$ on the basis of the equivalent reluctance network (Fig. 16), where R_t is the total reluctance for the total magnetic flux Φ (main flux Φ_g and leakage fluxes Φ_l). At 50 Hz, the measured and calculated magnetic flux densities are $B_0 = 0.15$ T. The magnetic flux density as function of the line voltage $V_L = 4\sqrt{3} V_{\mathrm{elm}}$ at 50 Hz is shown in Fig. 17. Measurements of B_0 have been performed using a gaussmeter with the Hall probe.

APPENDIX II
ENERGY CONSUMPTION

For the connection of the primary coils as in Fig. 3, the impedance of the primary system per phase with the secondary

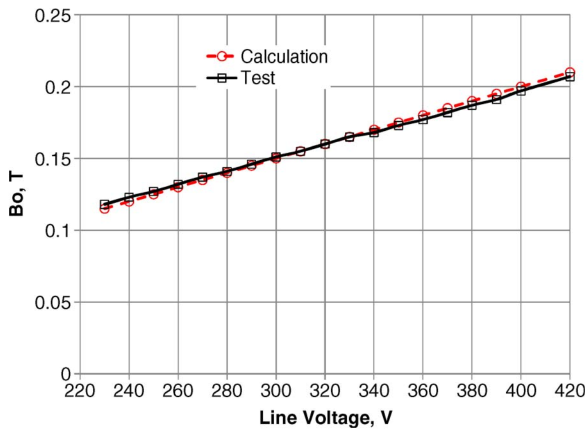

Fig. 17. Normal component of the magnetic flux density B_0 at the surface of the center leg in its center line ($f = 50$ Hz).

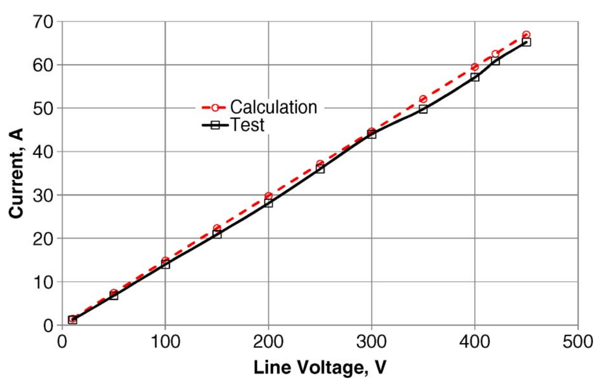

Fig. 18. Current versus line voltage at $f = 50$ Hz.

being removed is

$$\mathbf{Z_{ph}} = \frac{4}{3}(R_{\mathrm{elm}} + jX_{\mathrm{elm}}) \tag{50}$$

where $R_{\mathrm{elm}} = 0.543\ \Omega$ and $X_{\mathrm{elm}} = 2\pi \times 50 \times 0.0091 = 2.858\ \Omega$ are the resistance and reactance of the single electromagnet coil, respectively. There are three parallel paths with four coils in series per phase (Fig. 3).

The *rms* phase current I_{ph}, input apparent power S_{in}, input active (true) power P_{in}, and power factor $pf = cos\varphi$ are, respectively

$$I_{\mathrm{ph}} = \frac{V_L}{\sqrt{3}|\mathbf{Z_{ph}}|} \tag{51}$$

$$P_{\mathrm{in}} = 3I_{\mathrm{ph}}^2 \Re e[\mathbf{Z_{ph}}] \tag{52}$$

$$S_{\mathrm{in}} = \sqrt{3}V_L I_{\mathrm{ph}} \tag{53}$$

$$pf = \cos\varphi = P_{\mathrm{in}}/S_{\mathrm{in}}. \tag{54}$$

Steady-state characteristics $I_{\mathrm{ph}} = f(V_L)$, $P_{\mathrm{in}} = f(V_L)$, and $pf = f(V_L)$ obtained from calculations and measurements for an open magnetic circuit (no secondary) are plotted in Figs. 18–20.

Since the electromagnets have an open magnetic circuit, the presence of the nonferromagnetic secondary practically does not affect the current, input power, and power factor. The magnetizing current is much higher than eddy currents induced in the nonferromagnetic secondary, so that, in practice, the presence of the secondary does not affect the power consumption. The measured current, input active power, and power factor $\cos\varphi$ with the secondary and without the secondary are plotted in Figs. 21–23.

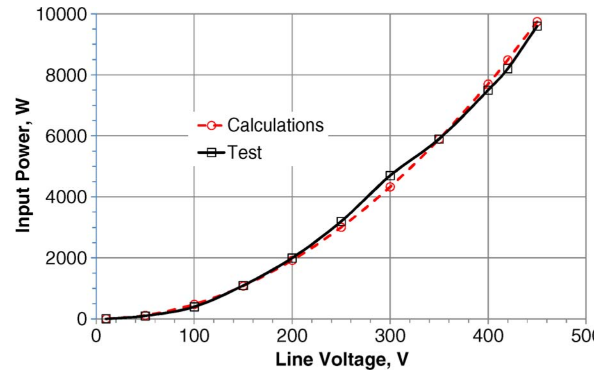

Fig. 19. Input active power versus line voltage at $f = 50$ Hz.

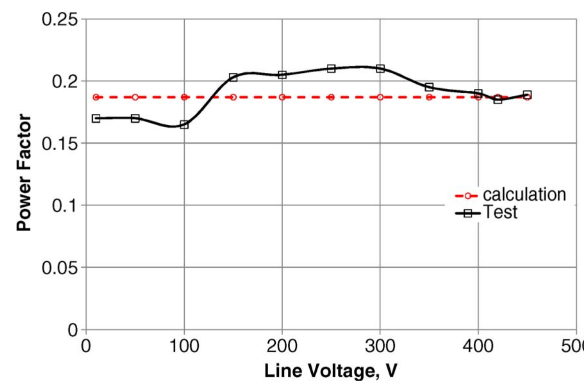

Fig. 20. Power factor $\cos\varphi$ versus line voltage at $f = 50$ Hz.

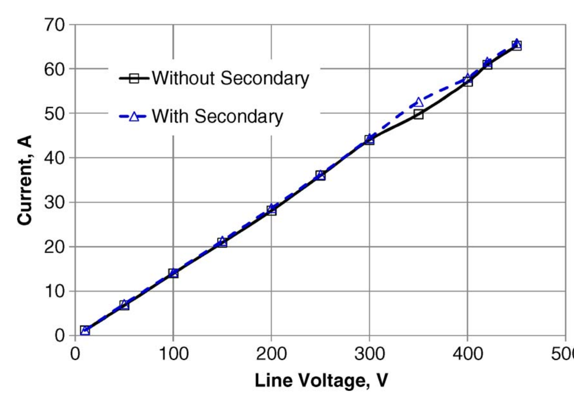

Fig. 21. Current versus line voltage without and with the secondary at $f = 50$ Hz. Test results.

APPENDIX III
COMPLEX PROPAGATION CONSTANT AND MAGNETIC PERMEABILITY

For a conductive medium, power frequencies, fundamental harmonic $\nu = 1$, and 1-D electromagnetic field, the complex

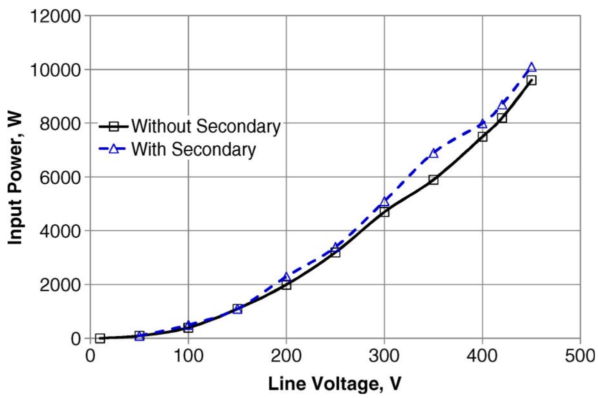

Fig. 22. Input active power versus line voltage without and with the secondary at $f = 50$ Hz. Test results.

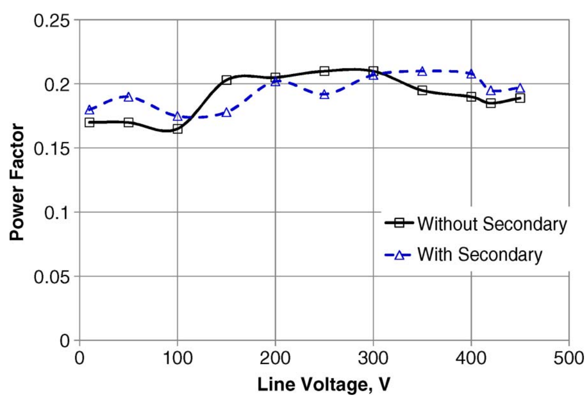

Fig. 23. Power factor $\cos\varphi$ versus line voltage without and with the secondary at $f = 50$ Hz. Test results.

propagation constant has the following general form [4]:

$$\alpha = (a_R + ja_x)k = \sqrt{(a_R^2 + 2ja_R a_X - a_X^2)\frac{\omega\mu_o\mu_{\rm rs}\sigma}{2}}$$
$$= \sqrt{2j}\sqrt{a_R a_X - j\frac{a_R^2 - a_X^2}{2}}\sqrt{\frac{\omega\mu_o\mu_{\rm rs}\sigma}{2}} \tag{55}$$

where $a_R \geq 1$, $a_X \leq 1$, and k is the attenuation factor of the electromagnetic field, i.e.,

$$k = \sqrt{\pi f \mu_0 \mu_{\rm rs}\sigma}. \tag{56}$$

In (56), μ_0 is the magnetic permeability of free space, $\mu_{\rm rs}$ is the relative surface magnetic permeability, and σ is the electric conductivity. To take into account magnetic saturation and hysteresis losses in ferromagnetic bodies, the relative magnetic permeability has a complex form [4], i.e.,

$$\mu_r = \mu_{\rm rs}(\mu' - j\mu''). \tag{57}$$

The following relationship exists between a_R, a_X, μ', and μ'':

$$\mu' = a_R a_X \qquad \mu'' = 0.5\left(a_R^2 - a_X^2\right). \tag{58}$$

For most mild steels, $a_R \approx 1.45$ and $a_X \approx 0.85$. For paramagnetic or diamagnetic bodies, $a_R = a_X = 1$. It means that $\mu' = 1$, $\mu'' = 0$, and complex propagation constant

$$\alpha = (1 + j)k = \sqrt{2j}k \tag{59}$$

since $2j = 1 + 2j - 1 = (1 + j)^2$.

Appendix IV
Angular Frequency in the Primary and Secondary

If the Cartesian coordinate system x, y, z (Fig. 8) moves in the x-direction with the linear velocity of the secondary $v_2 = v(1 - s)$, where $v = 2f\tau$ is the synchronous velocity and s is the slip for the fundamental harmonic $\nu = 1$, the slip for higher space harmonics $\nu > 1$ is as follows [9]:

- for forward-traveling field

$$s_\nu^+ = s_\nu = 1 - \nu(1 - s) \tag{60}$$

- for backward-traveling field

$$s_\nu^- = 2 - s_\nu = 1 + \nu(1 - s). \tag{61}$$

In the coordinate system moving with the velocity of the secondary, the time–spatial variation of all electric and magnetic quantities in the secondary is proportional to

$$\exp[j(\omega_{\nu 2} \mp \beta_\nu x)] \tag{62}$$

where

- for forward-traveling field

$$\omega_{\nu 2}^+ = \omega s_\nu^+ = \beta_\nu\left(\frac{\omega}{\beta_\nu} - v_2\right) \tag{63}$$

- for backward-traveling field

$$\omega_{\nu 2}^- = \omega s_\nu^- = \beta_\nu\left(\frac{\omega}{\beta_\nu} + v_2\right) \tag{64}$$

and

$$\omega = 2\pi f = \frac{\pi v}{\tau}. \tag{65}$$

Please note that the time-dependent factor $\exp(j\omega_{\nu 2})$ at both sides of (10)–(12) has been neglected. The stationary coordinate system x_0, y_0, z_0 and moving coordinate system x, y, z are linked by the following equation:

$$x_0 = x - v_2 t = x - \frac{v}{\nu}(1 - s_\nu)t = x - \frac{\omega}{\beta_\nu}(1 - s_\nu)t \tag{66}$$

while $y_0 = y$ and $z_0 = z$.

References

[1] J. S. Choi and Y. S. Baek, "Magnetically-levitated conveyance system using electromagnets and a linear induction motor," *IEEE Trans. Magn.*, vol. 44, no. 11, pp. 4171–4174, Nov. 2008.
[2] J. F. Eastham and E. R. Laithwaite, "Linear induction motors as electromagnetic rivers," *Proc. Inst. Elect. Eng.*, vol. 121, no. 10, pp. 1099–1108, Oct. 1974.
[3] E. M. Freeman and D. A. Lowther, "Normal force in single-sided linear induction motors," *Proc. Inst. Elect. Eng.*, vol. 120, no. 12, pp. 1499–1506, Dec. 1973.

[4] J. F. Gieras, “Analytical method of calculating the electromagnetic field and power losses in ferromagnetic halfspace, taking into account saturation and hysteresis,” *Proc. Inst. Elect. Eng.*, vol. 124, no. 11, pp. 1098–1104, 1977.

[5] J. F. Gieras, “Electrodynamic forces in electromagnetic levitation systems,” *Acta Technica CSAV*, no. 5, pp. 532–545, 1982.

[6] J. F. Gieras, “Influence of structure and material of secondary suspended electrodynamically on steady performance characteristics of LIM with transverse flux,” *etzArchiv*, vol. 6, no. 7, pp. 255–260, 1984.

[7] J. F. Gieras, “Transverse flux electrodynamic levitation system,” in *Proc. Int. Conf. Maglev Transp.*, Tokyo, Japan, 1985, pp. 207–215.

[8] J. F. Gieras, “Analysis of multilayer rotor induction motor with higher space harmonics taken into account,” *Proc. Inst. Elect. Eng.—Elect. Power Appl.*, vol. 138, no. 2, pp. 59–67, Mar. 1991.

[9] J. F. Gieras, *Linear Induction Drives*. Oxford, U.K.: Clarendon, 1994.

[10] J. F. Gieras, Z. J. Piech, and B. Z. Tomczuk, *Linear Synchronous Motors: Transportation and Automation Systems,* 2nd ed. New York: Taylor & Francis, 2011.

[11] H. Hayashiya, H. Ohsaki, and E. Masada, “A combined lift and propulsion system of a steel plate by transverse flux linear induction motors,” *IEEE Trans. Magn.*, vol. 35, no. 5, pp. 4019–4021, Sep. 1999.

[12] P. Hochhausler, “Der Katamaran als magnetisches Schwebefahrzeug,” *ETZ B*, vol. 26, no. 3, pp. 412–413, 1973.

[13] B. V. Jayawant, *Electromagnetic Levitation and Suspension Techniques*. London, U.K.: E. Arnold, 1981.

[14] C. T. Liu, Y. Y. Yang, and S. Y. Lin, “Development of an automatic online gap-detection scheme for levitated industrial steel-plate conveyance system,” *IEEE Trans. Ind. Appl.*, vol. 44, no. 2, pp. 517–524, Mar./Apr. 2008.

[15] J. Turowski, *Fundamentals of Mechatronics*. Łódź, Poland: WSHE, 2008.

Jacek F. Gieras (M’83–SM’87–F’02) received the M.Eng. degree (with distinction) from the Technical University of Lodz, Lodz, Poland, in 1971, and the Ph.D. degree in electrical engineering (electrical machines) and the Dr. Habil. degree (corresponding to the D.Sc. degree) in electrical engineering from Poznan University of Technology, Poznan, Poland, in 1975 and 1980, respectively.

In 1987, he was promoted to the rank of Full Professor (a life title given by the President of the Republic of Poland). Since 1998, he has been with United Technologies Corporation, Hartford, CT, where, most recently, he has been with Hamilton Sundstrand Applied Research. Since 2007, he has been a Faculty Member (Full Professor) in the Department of Electrical Engineering, University of Technology and Life Sciences, Bydgoszcz, Poland. He has authored or coauthored 11 books and over 250 scientific and technical papers and is the holder of 70 U.S. patents and patent publications. His most important books are *Linear Induction Drives* (Oxford University Press, 1994), *Permanent Magnet Motor Technology: Design and Applications* (Marcel Dekker Inc., 1996; Marcel Dekker Inc., 2002; and Taylor & Francis, 2010), *Linear Synchronous Motors: Transportation and Automation Systems* (CRC Press, 1999 and 2011), *Axial Flux Permanent Magnet Brushless Machines* (Springer–Kluwer Academic, 2004 and 2008) (with coauthors R.Wang and M. J. Kamper), *Noise of Polyphase Electric Motors* (CRC Press–Taylor & Francis, 2005) (with coauthors C. Wang and J. C. Lai), and *Advancements in Electric Machines* (Springer, 2008). His research areas include electrical machines, drives, electromagnetics, power systems, and railway engineering.

Prof. Gieras is a Hamilton Sundstrand Fellow (United Technologies Corporation), a full member of the International Academy of Electrical Engineering, and a member of the steering committees of numerous international conferences.

Jacek Mews received the B.S. degree in electrical engineering from the University of Technology and Life Sciences, Bydgoszcz, Poland, in 2009, where he is currently working toward the M.Eng. degree in the Department of Electrical Engineering.

He is also currently a Manager with the Technology Department, Gzelle Ltd., Osie, Poland.

Pawel Splawski received the B.S. degree in electrical engineering from the University of Technology and Life Sciences, Bydgoszcz, Poland, in 2009.

He is currently an Operating Engineer of power plants with Saturn Management Ltd., Swiecie, Poland.